MODULATED LUMINESCENCE TOMOGRAPHY

PLAMEN STEFANOV, WENXIANG CONG, AND GE WANG

ABSTRACT. We propose and analyze a mathematical model of Modulated Luminescent Tomography. We show that when single X-rays or focused X-rays are used as an excitation, the problem is similar to the inversion of weighted X-ray transforms. In particular, we give an explicit inversion in the case of Dual Cone X-ray excitation.

1. INTRODUCTION: A BRIEF DESCRIPTION OF THE METHOD AND THE MODEL

1.1. **A brief description of the modalities.** The purpose of this work is to build and analyze the mathematical model of several medical multiwave imaging techniques that we call Modulated Luminescent Tomography. Certain phosphorescent contrast agents (for example, nanophosphors) are delivered to the cells and then illuminated with X-rays. The illuminated particles emit photons which scatter through the tissue and are detected outside the body, see, e.g., [7]. The goal is to recover the concentration of the contrast agents. When a contrast agent is used for molecular imaging, involved nanoparticles are functionalized to target specific cellular features. As a result, the concentration of the contrast agent will be directly correlated to the distribution of the targeted biomarkers, enabling quantitative analysis to guide molecular/individualized medicine. The resolution of this modality is expected to come from the X-ray excitation. In this respect, those modalities behave differently than Photoacoustic and Thermoacoustic Tomography, where the excitation is highly diffusive but the emitted ultrasound signal allows for high resolution, see, e.g., [5, 17]; and [6, 15] and the references there for the analysis of the mathematical model.

Two such techniques, X-ray luminescence computed tomography (XLCT) [11] and X-ray micro-modulated luminescence tomography (XMLT) [2, 1], described below, have been proposed recently. They combine X-ray focusing, nanophosphor excitation, optical sensing, and image reconstruction in a synergistic fashion, and promise significant imaging performance gains in both microscopic and preclinical studies. The XMLT approach is an exogenous reporter-based imaging system in which spatial resolution is determined by the excitation of the luminescence from nanophosphors with a micro-focused X-ray beam such as a zone-plane or a micro-focus X-ray source coupled with a polycapillary lens. High in vivo spatial resolution can be achieved due to the short wavelength and small spot size of the X-rays. When X-rays are focused in this way, double cones of X-rays are formed with their shared vertex point inside a sample or a subject. Those modalities are proposed as alternatives to fluorescence molecular tomography (FMT) and bioluminescence tomography (BLT) [9, 16] in order to improve resolution and stability.

In X-ray luminescence CT (XLCT), a pin-hole collimator is used to restrict x-rays into a pencil beam for excitation of nanophosphors, based on the particle nature of x-rays. Due to the mechanical limitations of a pin-hole collimator as well as the scattering and diffraction effects of X-rays, this imaging method can hardly achieve sub-micron-scale spatial resolution. On the other hand, X-ray micro-modulated luminescence tomography (XMLT), X-rays are focused onto a micron-scale focal spot using a polycapillary lens or a zone plate, based on the wave nature of X-rays. Hence,

the focusing X-rays excite nanophosphors and improve spatial resolution dramatically. Combining optical sensitivity and X-ray resolution, XMLT potentially allows a significant gain in the imaging performance in terms of spatial resolution, contrast concentration, and penetration depth, relative to what is currently available other optical imaging methods, see also Figure 2 in [8].

Our main results state that we can use boundary averaged measurements only and the problem is reduced to an inversion of a weighted linear transform determined by the excitation. For example, if the excitation consist of single X-rays, in Section 5, we get a weighted X-ray transform with a weight depending on the diffusion and the absorption coefficients D and μ_a of the medium with respect to the emitted photons, see (1.2) below. In the case of double cone excitation (XMLT) with a constant aperture, or in XLCT, we have an explicit and stable inversion under an explicit if and only if condition, see (4.3), Theorem 4.1 and Section 4. We show that the local problem in a region of interest behaves similarly to the corresponding X-ray problems, and we have explicit microlocal inversions of the visible singularities.

1.2. The model.
Let $\Omega \subset \mathbf{R}^n$ be a smooth domain. We illuminate the medium in different ways. Each illumination excites the particles at a rate $I_\alpha(x)$, which can be a distribution, where α belongs to some index set $\mathcal{A}$, discrete or not. In the X-ray case, $I_\alpha(x)$ is just a superposition of delta functions along straight lines; which also allows for attenuated X-rays by introducing an appropriate weight. The structure of I_α is not important at the moment; see section 4 and section 5 for the cases XLCT and XMLT. The modulated source then is

$$(1.1) \qquad\qquad s_\alpha(x) = I_\alpha(x)f(x),$$

where f is the concentration of the active particles, which we want to reconstruct. We assume that the light from the source propagates according to the diffusion model [18]

$$(1.2) \qquad\qquad (-\nabla \cdot D\nabla + \mu_a)\, u_\alpha = s_\alpha(x) \quad \text{in } \Omega.$$

Here, $\mu_a(x) \geq 0$ is the absorption, $D(x) > 0$ is the diffusion coefficient, and u_α is the photon density. The coefficients μ_a and D are given. In the diffusion approximation regime, $D(x) = [3(\mu_a + \mu_s')]^{-1} > 0$, where $\mu_s' = (1-g)\mu_s$ is the reduced scattering coefficient, μ_s is the scattering coefficient and g is the scattering anisotropy.

The boundary conditions are of semi-transparent type due to the different index of refraction of the tissue and the air around it. They are of Robin type and have the form

$$(1.3) \qquad\qquad u_\alpha + 2AD\partial_\nu u_\alpha\big|_{\partial\Omega} = 0,$$

where $A > 0$ is a given coefficient, well approximated by $A = (1 + R)/(1 - R)$ with R closely approximated by $R = -1.4399m^{-2} + 0.7099m^{-1} + 0.6681 + 0.063m$ [13], where m is the refractive index of the tissue. Let G be the solution operator (the Green's function) of (1.2), (1.3), i.e., $u_\alpha = Gs_\alpha = GI_\alpha f$.

What we measure is the outgoing photon density

$$(1.4) \qquad\qquad Q_\alpha f = -D\partial_\nu u_\alpha\big|_{\partial\Omega} = \frac{1}{2A}u_\alpha|_{\partial\Omega} = \frac{1}{2A}(GI_\alpha f)|_{\partial\Omega}.$$

The data therefore is

$$\{Q_\alpha f\}_{\alpha\in\mathcal{A}},$$

and we want to reconstruct f. For each illumination choice, α, the data Q_α is a function of $n-1$ variables. When α runs over a continuous space with dimension m, we get $m+n-1$ variables. This could make the problem formally overdetermined. On the other hand, because of the diffusion nature of the data for a fixed α, we cannot have much resolution hidden in that Q_α. The only way to get resolution (i.e., stability) is to have a well chosen set of illuminations I_α, $\alpha \in \mathcal{A}$ which have enough singularities. We show below that we do not actually need to know or measure Q_α pointwise; some average over $\partial\Omega$ is enough for a stable recovery. This removes $n-1$ variables from the data.

2. The first phase: recovery of an averaged intensity.

2.1. **The general case.** The operator $L := -\nabla \cdot D\nabla + \mu_a$ is symmetric and positive on smooth functions satisfying the the Robin boundary condition (1.3) because

$$
\begin{aligned}
\int_\Omega (Lu)\bar{u}\,\mathrm{d}x &= \int_\Omega \left(|\nabla u|^2 + \mu_a|u|^2\right)\mathrm{d}x - \int_{\partial\Omega}(\partial_\nu u)\bar{u}\,\mathrm{d}\sigma \\
&= \int_\Omega \left(|\nabla u|^2 + \mu_a|u|^2\right)\mathrm{d}x + \int_{\partial\Omega}\frac{1}{2AD}|\bar{u}|^2\,\mathrm{d}\sigma,
\end{aligned}
\tag{2.1}
$$

where $\mathrm{d}\sigma$ is the surface measure. By Green's formula, for such u and v,

$$
\begin{aligned}
\int_\Omega (\bar{v}Lu - uL\bar{v})\,\mathrm{d}x &= -\int_{\partial\Omega}(\bar{v}\partial_\nu u - u\partial_\nu\bar{v})\,D\,\mathrm{d}\sigma \\
&= -\int_{\partial\Omega}\left((\bar{v}+2AD\partial_\nu\bar{v})\partial_\nu u - (u+2AD\partial_\nu u)\partial_\nu\bar{v}\right)D\,\mathrm{d}\sigma = 0.
\end{aligned}
\tag{2.2}
$$

Therefore, L with the Robin boundary conditions if symmetric and positive by (2.1). It is well known that L extends to a self-adjoint operator on $L^2(\Omega)$ with a compact resolvent, see, e.g., [12, Theorem X.23]. In particular, 0 is in the resolvent set by (2.1). This shows that the Green's function G is well-defined, and self-adjoint on $L^2(\Omega)$. Moreover, the boundary-value problem (2.4) below is well posed.

If $Lv_\alpha = 0$, and u_α solves (1.2), (1.3), we get (we drop the index α in this formula)

$$
\begin{aligned}
\int_\Omega vs\,\mathrm{d}x &= -\int_{\partial\Omega}(v\partial_\nu u - u\partial_\nu v)\,D\,\mathrm{d}\sigma = -\int_{\partial\Omega}(v+2AD\partial_\nu v)\,D\partial_\nu u\,\mathrm{d}\sigma \\
&= \int_{\partial\Omega}(v+2AD\partial_\nu v)\,Qf\,\mathrm{d}\sigma.
\end{aligned}
\tag{2.3}
$$

This suggests the following. Choose h_α regular enough, and let $v_\alpha =: Vh_\alpha$ solve

$$
\begin{aligned}
(-\nabla \cdot D\nabla + \mu_a)\,v_\alpha &= 0 \quad \text{in } \Omega, \\
v_\alpha + 2AD\partial_\nu v_\alpha\big|_{\partial\Omega} &= h_\alpha.
\end{aligned}
\tag{2.4}
$$

Then, by (2.3),

$$
\int_\Omega v_\alpha I_\alpha f\,\mathrm{d}x = \int_{\partial\Omega} h_\alpha Q_\alpha f\,\mathrm{d}\sigma.
\tag{2.5}
$$

In other words, choose h_α somehow; then we can recover $\int_\Omega (Vh_\alpha)I_\alpha f\,\mathrm{d}x$ from the data. This requires us to solve (2.4) first but this can be done numerically in a very efficient way. If D and μ_a are constants, and Ω is a circle or a rectangle, it can be done explicitly, as we show below. This gives us a way to compute an averaged value of $I_\alpha f$, with a weight v_α depending on the choice of h_α. If $\mu_a = 0$, one can take $h_\alpha = 1$ and then $v_\alpha = 1$. We would want to have positive solutions $v > 0$, and we do not want $v \ll 1$ because we will divide by it eventually, see Theorem 4.1. Positivity can be guaranteed by the maximum principle if $h > 0$, see Lemma 2.1 below. The lower bound of u could be very small if the attenuation μ_a is large, and that would create stability problems; but this is natural to expect. Fortunately, this is not the case for imaging of small animals, for example; a realistic value for μ_a and for the size of Ω is presented in Section 6.

Lemma 2.1. *Let $0 < h \in C^2(\partial\Omega)$ and let v be the solution of (2.4) with the subscript α there dropped. Then*

$$
0 < v(x) \leq \max_{\partial\Omega} h, \quad \forall x \in \bar{\Omega}.
$$

Proof. Assume that the first inequality is false. Then there exists a point $x_0 \in \bar{\Omega}$ where v attains a minimal value $v_0 = v(x_0) < 0$. If x_0 is interior for Ω, then $v = \text{const.}$ by the maximum principle, see [3, p. 333], therefore, $v(x) = v_0 < 0$. By the boundary condition, $h = v_0$ as well which contradicts

the assumption $h > 0$. Therefore, $x_0 \in \partial\Omega$. By the boundary condition again, $\partial_\nu v(x_0) > 0$. This means that there is an interior point where v takes a strictly smaller value which is a contradiction.

On the other hand, at a point $y_0 \in \partial\Omega$, where v achieves its maximum, that maximum has to be less or equal than $h_\alpha(y_0)$ because otherwise, $\partial_\nu v_\alpha(y_0)$ would be negative; and that would violate the classical maximum principle, see [3, p. 239]. Therefore $\max_{\bar\Omega} v = \max_{\partial\Omega} v \leq h(y_0) \leq \max h$.   □

Note that we do not need to solve the boundary value problem (2.4) to find v. We could just take any solution v of $(-\nabla \cdot D\nabla + \mu_a)v = 0$ and compute $h = (v + 2AD\partial_\nu v)\big|_{\partial\Omega}$ next. If D and μ_0 are constants, we can generate many explicit solutions, regardless of the shape of the domain.

Finally, we want to emphasize that we cannot recover $s_\alpha = I_\alpha f$ from (2.5) known for all h_α; for example, for any $\phi \in C_0^\infty(\Omega)$, adding $L\phi$ to $I_\alpha f$ would not change the left-hand side of (2.5).

We consider the constant coefficient cases below and continue with the general case in the next section.

2.2. Partial cases: D and μ_a constants.
Assume now that $D > 0$ and $\mu_a \geq 0$ are constants.

2.3. $n = 3$, Ω a ball.
Let $n = 3$. The (exponentially decreasing) Green's function of $L = -D\Delta + \mu_a$ is then given by

$$(2.6) \qquad\qquad G_k(x, y) = \frac{e^{-k|x-y|}}{4\pi D|x - y|},$$

with $k = \sqrt{\mu_a/D}$, i.e., $(-D\Delta_x + \mu_a)G(x, y) = \delta(x - y)$ Then G_{-k} is a Green's function as well, and the difference is in the kernel of L. Therefore,

$$(-D\Delta_x + \mu_a)\frac{\sinh(k|x - y|)}{|x - y|} = 0.$$

Therefore, we can chose

$$(2.7) \qquad\qquad v(x) = \frac{\sinh(k|x - y|)}{|x - y|}$$

with y arbitrary but fixed. Then compute h from (2.4).

If Ω is the ball $\Omega = \{x|\ |x| \leq a\}$, then we can choose $y = 0$ to get

$$(2.8) \qquad v(x) = \frac{\sinh(k|x|)}{|x|}, \quad h = a^{-1}\sinh(ka) + 2AD\left(ka^{-1}\cosh(ka) - a^{-2}\sinh(ka)\right).$$

Note that h is just a constant on the boundary $|x| = a$. Then by (2.5), we can recover

$$\int_{|x|\leq a} I_\alpha(x)f(x)\frac{\sinh(k|x|)}{|x|}\,\mathrm{d}x.$$

When $ka \gg 1$, the function v is very small near 0 compared to its boundary values, which means poor recovery of s_α there (we do not actually recover s_α here, just a weighed integral of it). That can be expected though — signals coming from the center would be attenuated the most.

2.4. $n = 3$, Ω arbitrary.
One can still use v as in (2.8) (or, as in(2.7), see the remark above); then h needs to be calculated by the second equation in (2.4).

2.5. $n = 2$**,** Ω **a disk.** In this case, the fundamental solution involves the Bessel function K_0 and is $K_0(k|x - y|)$. Here, $K_0 = CH^{(1)}(ix)$ with some constant C and $H_0^{(1)}$ is the Hankel function of fist kind. Note that there is a weak (logarithmic) singularity at $x = y$. This is equivalent to (2.6) in the 3D case. One can then take

$$v(x) = I_0(k|x|),$$

where I_0 is the corresponding modified Bessel function of third kind, and there is no singularity. This is equivalent to taking $\sinh(k|x|)/|x|$ in 3D. For h on the sphere $|x| = a$ the boundary of the ball), we get

$$h = I_0(ak) + 2ADI_1(ak),$$

which is a constant again.

3. Reducing the problem to the invertibility of a weighted version of the illumination transform

As we showed above, we cannot recover the source $s_\alpha = I_\alpha f$ from (2.5). We are not trying to reconstruct s_α however. We view (2.5) as a linear integral transform

$$(3.1) \qquad\qquad R : f \longmapsto Rf(\alpha) := \int_\Omega v_\alpha I_\alpha f \, dx, \quad \alpha \in \mathcal{A}.$$

We can write equation (2.5) then as

$$(3.2) \qquad\qquad Rf(\alpha) = \int_{\partial\Omega} h_\alpha Q_\alpha f \, d\sigma.$$

The right-hand side is determined by the data. The goal then is to invert R. Recall that we have some freedom to choose $v_\alpha = V h_\alpha$, and in particular, we can choose them independently of α. Then v just multiples f, and we need to invert the transform with kernel $I_\alpha(x)$; and then divide by v.

We consider two main examples below: when R is a dual cone transform modeling the XMLT; and when R is a weighted X-ray transform, which models the XLCT.

4. Double cone excitation (XMLT)

4.1. Formulation. We work in $\mathbf{R}^n$ but the interesting case is $\mathbf{R}^3$. The idea of the XMLT is to focus X-rays, thus forming a double cone, at each point x in some region of interest ROI at N different directions θ_j, $j = 1, \ldots, N$. Then

$$\alpha = (x, j) \in \Omega \times \{1, 2, \ldots, N\}.$$

We model the cones with their aperture functions $a_{x,j}(\theta)$, $\theta \in S^{n-1}$, in other words, $I_\alpha(x)$ is a superposition of X-rays with density $a_{x,j}$. Then the corresponding intensity $I_{x,\alpha}(y)$ is given by

$$I_{x,j}(y) = \frac{a_{x,j}\left(\frac{x-y}{|x-y|}\right)}{|x - y|^{n-1}}.$$

For example, if we assume uniform angular density, then $a_{x,j}$ would be constant on the intersection of the interior of the cone with the unit sphere, and zero otherwise. We assume that the cones are double; then $a_{x,j}$ are even functions on the sphere. The simplest case is when $a_{x,j}$ is independent of x, and a_{x_1,j_1} is obtained from a_{x_2,j_2} by a translation in the x variable and a rotation in the angular one.

By (1.1), the transform R becomes

$$(4.1) \qquad\qquad Rf(x, j) = \int_\Omega \frac{a_{x,j}\left(\frac{x-y}{|x-y|}\right)}{|x - y|^{n-1}} v_{j,x}(y) f(y) \, dy.$$

If $a_{x,j}$ are smooth functions, then R is a ΨDO of order -1 with principal symbol

$$r_j(x,\xi) := \pi \int_{S^{n-1}} a_{x,j}(\theta) v_{j,x}(x) \delta(\xi \cdot \theta) \, d\theta,$$

see, e.g., [4]. Here, δ is the Dirac delta "function"; therefore, the integral is taken over the sphere of co-dimension two (the great circle if $n = 3$, two points if $n = 2$) of the unit sphere intersected with the plane normal to ξ. Note that the symbol above is homogeneous of order -1. This shows that the "visible" set of singularities $\mathcal{U} \subset T^*\Omega \setminus 0$ is where the system $\{r_j\}_{j=1}^N$ is elliptic, i.e.,

(4.2) $$\mathcal{U} = \{(x,\xi) \in T^*\Omega \setminus 0; \ \exists j, \theta \perp \xi \text{ so that } a_{x,j}(\theta) \neq 0\}.$$

4.2. **Recovery of the singularities in a region of interest.** If $\Omega_0 \subset \Omega$ is an open subset (a region of interest), and if $a_{x,j}$ are smooth, we can recover the singularities of f there, if the condition for $\mathcal{U}$ in (4.2) is satisfied for any $x \in \Omega_0$, i.e., if

(4.3) $$T^*\Omega_0 \setminus 0 \subset \mathcal{U}.$$

This can be done constructively as follows.

- For any j and $x \in \Omega_0$, choose a smooth function $0 < h_{j,x}$ on $\partial\Omega$ and compute $v_{j,x} = Vh_{j,x}$ by solving (2.4) with $h_\alpha = h_{j,x}$. This determines the transform R.
- Compute the right-hand side of (3.2) for $x \in \Omega_0$.
- In (3.2), apply a left parametrix for the matrix operator $f \mapsto Rf(j, \cdot)$ in Ω_0.

One way to construct a parametrix of order 1 is to construct a ΨDO with the following principal symbol

$$q_j := \left(\sum_k r_k^2\right)^{-1} r_j,$$

and then $\sum_j q_j(x, D)Rf(j, x) = f + Kf$, where K is of order -1. If $a_{x,j} \geq 0$, one can use instead

$$q := \left(\sum_k r_k\right)^{-1}$$

and then $q(x, D) \sum_j Rf(j, x) = f + Kf$ with K as above.

Note that we can simply choose $h_{j,x}$ independent of j, x.

The aperture functions $a_{x,j}$ only need to be smooth of finite order to recover the leading singularities, like jumps across surfaces. In practical implementations, this condition can be satisfied approximately by introducing vignetting near the edges of the cones. Even without applying the operator Q, the $\sum_j Rf(j, x)$ would recover all singularities in the correct places but with varying amplitudes. Below, we consider a practical case where $a_{x,j}$ are enough to be L^∞ only.

When the stability condition (4.3) does not hold, we can still reconstruct the visible singularities in $\mathcal{U}$ stably by a microlocal inversion, if $a_{x,j}$ are smooth but not the ones in the complement of $\bar{\mathcal{U}}$, see, e.g., [14].

4.3. **Explicit global inversion when the apertures are translation-independent.** Assume now that the aperture functions are non-negative and independent of x, i.e., they are given by $a_j(\theta)$. This is the actual experimental case, actually. The stability condition (4.3) then takes the following form, see (4.2) :

(4.4)   Any plane through the origin intersects at least one of the cones $\{\theta; \ a_j(\theta) > 0\}$.

Assume also that $h_{j,x}$ are independent of j and x. The construction above then simplifies as follows. We have

$$r_j(x,\xi) := r_j^0(\xi)v(x), \quad r_j^0(\xi) := \pi \int_{S^{n-1}} a_j(\theta)\delta(\xi \cdot \theta) \, d\theta,$$

and $r_j(\xi)v(y)$ is actually the full (not just the principal symbol) amplitude of $f \mapsto Rf(j, \cdot)$. Symbols independent of x are Fourier multipliers, i.e., $r_j(D) = \mathcal{F}^{-1}r_j\mathcal{F}$, where $\mathcal{F}$ is the Fourier transform.

Then $R_j = r_j^0(D)v$ with v regarded as a multiplication, where we changed the notation for R since $\alpha = j$ now. In integral form,

$$R_j f(x) = \int_\Omega \frac{a_j\left(\frac{x-y}{|x-y|}\right)}{|x-y|^{n-1}} v(y) f(y) \, \mathrm{d}y.$$

Note that $r_j^0(D)$ makes sense even if a_j is L^∞ only.

Equation (3.2) takes the form

$$R_j f(x) = \int_{\partial\Omega} h Q_{j,x} \, \mathrm{d}\sigma.$$

When the stability condition (4.4) holds, this equation can be solved explicitly as follows

(4.5) $$f = \frac{1}{v}\left(\sum_j r_j(D)\right)^{-1} \sum_j \int_{\partial\Omega} h Q_{j,x} \, \mathrm{d}\sigma.$$

We summarize this in the following:

Theorem 4.1. *Let the aperture functions $0 \le a_j(\theta) \in L^\infty$ be independent of the point x where we focus. Choose $0 < h \in C^2(\partial\Omega)$ and let $v = Vh$ be the solution of (2.4) corresponding to that h. If the stability condition (4.4) holds, then f can be explicitly computed by (4.5).*

Moreover,

$$\|f\|_{L^2(\Omega)} \le C \frac{\max_{\partial\Omega} h}{\min_{\bar\Omega} v} \left\| \int_{\partial\Omega} \sum_j Q_{j,x} \, \mathrm{d}\sigma \right\|_{H^1(\Omega_x)}.$$

The subscript x in Ω_x indicates that the H^1 norm is taken w.r.t. to the variable x. We used Lemma 2.1 to conclude that v has a positive minimum.

Remark 4.1. One way to satisfy the stability condition (4.4) is to make sure that union of the open sets $\{a_j > 0\}$ where the apertures do not vanish covers the equator of the unit sphere (or any great circle fixed in advance). This is the situation in the numerical example below. If the apertures $\{a_j > 0\}$ are too small, then there will be a large variation between the minimum and the maximum of the symbol q below, which may lead to a mild instability; the most stable singularities would be the vertical ones.

5. X-ray excitation (XLCT)

In the X-ray excitation case, we send individual X-rays through the medium. If the direction is $\theta \in S^{n-1}$, and we parameterize lines in this direction by initial points z on $\theta^\perp = \{x; \; x \cdot \theta = 0\}$, we have

$$\alpha = (\theta, z), \quad \theta \in S^{n-1}, \; z \in \theta^\perp.$$

In other words, we identify the directed lines in $\mathbf{R}^n$ with such α's. Then I_α is just a delta unction on the line parameterized by α. Therefore, R is just the weighted X-ray transform with weight $h_{\theta,z}$. Assume now that h is chosen independently of the line parameterized by (θ, z). Then

$$Rf = R_0 vf, \quad R_0 g(\theta, z) = \int g(z + t\theta) \, \mathrm{d}t.$$

Equation (3.2) takes the form

$$(R_0 vf)(\theta, z) = \int_{\partial\Omega} h Q_{\theta,z} \, \mathrm{d}\sigma.$$

In other words, each measurement gives us an integral of vf over a single line. The function f can then be found by inverting the X-ray transform R_0 and then dividing by v. The problem with a subset of lines and microlocal recovery in a ROI is the same as with the X-ray transform. Note that in practice, diffraction and other engineering challenges limit the ability to concentrate the radiation too closely along a single line thus limiting the resolution.

6. Numerical simulations

A spherical phantom of radius 10 mm was employed for the numerical simulation. The phantom is assigned with optical parameters: absorption coefficient $\mu_a = 0.05$ mm^{-1}, scattering coefficient $\mu_s = 15.0$ mm^{-1}, anisotropic coefficient $g = 0.9$, and relative refractive index of 1.37. The phantom was discretized into $65,775$ tetrahedral elements and $12,044$ nodes. A total of $2,108$ virtual detectors were distributed over the phantom surface to record the photon fluence rates. Then two light sources of radius 1.0 mm were embedded into the phantom, and filled with nanophosphors of concentrations of 5 μg/mL and 10 μg/mL, respectively. The centers of the two light sources were at $(2.5, 2.5, 0.0)$ and $(3.5, 0.0, 0.0)$. Two spherical subregions have a separation of 0.69 mm to test the spatial resolution. Using a polycapillary lens, X-ray beams are reshaped to double cone with a cone angle of 19.2 degrees. The focal point of the X-ray is scanned at grid points in a region of interest ROI $= \{-2 < x < 5, \ -2 < y < 5, \ -2 < z < 2\}$ along a scanning direction. Then, the phantom was rotated with 10 equal angles over a 360 degrees range to acquire sufficient information for an improved stability of the reconstruction. The stability condition (4.4) then holds, see Remark 4.1.

At each scanning, the intensity of the photon luminescence on the surface of the phantom was acquired. The intensity describes the optical emission of nanophosphors with double cone excitation. The intensity of the near-infrared radiation on the surface of the phantom can be simulated according to the diffusion approximation model. The intensity data are used as mean values of Poisson distribution to generate the simulated measurement data with Poisson noise. After discretization, the LSQR method [10] was used to solve the resulting system, in order to reconstruct the nanophosphor distribution from simulation data. The reconstructed results are in excellent agreement with the true phantom, and the average relative error of the reconstructed nanophosphor concentration was less than 5.37%, which was defined as

$$\text{Error} = \frac{1}{\#\{i|\ \rho_i^T > \epsilon\}} \sum_{\rho_i^T > \epsilon} \frac{\rho_i^r - \rho_i^T}{\rho_i^T},$$

where ρ_i^T and ρ_i^r are the true and reconstructed nanoparticles concentrations, respectively, and ϵ is a background noise level with a value of 0.1 μg/mL. Figures 1–2 present the comparison between the true and reconstructed nanophosphor distribution, showing the quantification accuracy of the image reconstructions.
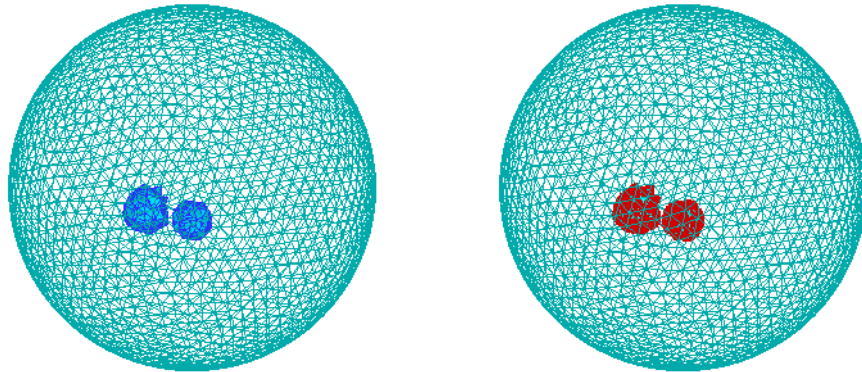

FIGURE 1. Modulated luminescence tomography 3D simulation. Left: the true nanophosphor distribution in the phantom. Right: the reconstructed nanophosphor distribution. The different colors on left and right do not represent different values.
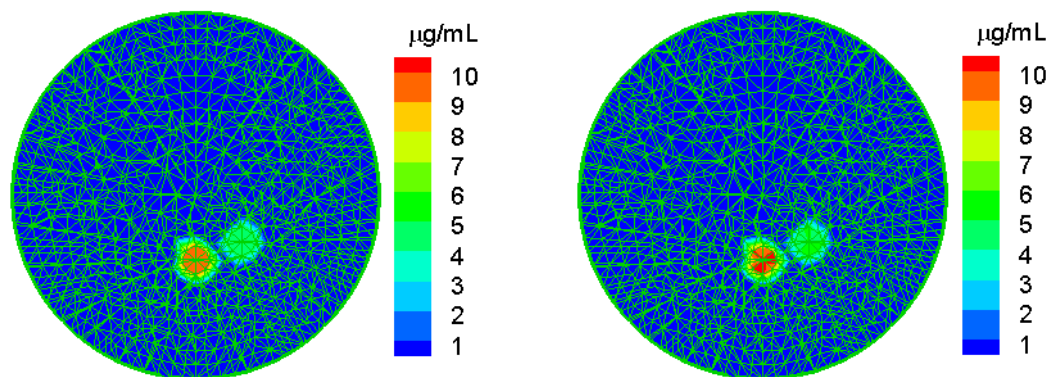
FIGURE 2. Modulated luminescence tomography simulation. Left: The true nanophosphor distribution on the 2D slice $z = 0$. Right: the reconstructed nanophosphor distributionat on the 2D slice $z = 0$.

REFERENCES

1. W Cong, Z Pan, R Eilkins, A Srivastava, N Ishaque, P Stefanov, and Ge Wang, *X-ray micromodulated luminescence tomography in dual-cone geometry*, Journal of Biomedical Optics **to appear** (2014).

2. Wenxiang Cong, Fenglin Liu, Chao Wang, and Ge Wang, *X-ray micro-modulated luminescence tomography (XMLT)*, Opt. Express **22** (2014), no. 5, 5572–5580.

3. Lawrence C. Evans, *Partial differential equations*, Graduate Studies in Mathematics, vol. 19, American Mathematical Society, Providence, RI, 1998. MR MR1625845 (99e:35001)

4. Bela Frigyik, Plamen Stefanov, and Gunther Uhlmann, *The X-ray transform for a generic family of curves and weights*, J. Geom. Anal. **18** (2008), no. 1, 89–108.

5. R. A. Kruger, D. R. Reinecke, and G. A. Kruger, *Thermoacoustic computed tomography–technical considerations.*, Med Phys **26** (1999), no. 9, 1832–1837.

6. Peter Kuchment and Leonid Kunyansky, *Mathematics of thermoacoustic tomography*, European J. Appl. Math. **19** (2008), no. 2, 191–224. MR MR2400720

7. Feng Liu, Wuzhao Yan, Yen-Jun Chuang, Zipeng Zhen, Jin Xie, and Zhengwei Pan, *Photostimulated near-infrared persistent luminescence as a new optical read-out from Cr^{3+}-doped $LiGa_5O_8$.*, Sci Rep **3** (2013), 1554 (eng).

8. Vasilis Ntziachristos, *Going deeper than microscopy: the optical imaging frontier in biology.*, Nat Methods **7** (2010), no. 8, 603–614 (eng).

9. Vasilis Ntziachristos, Jorge Ripoll, Lihong V. Wang, and Ralph Weissleder, *Looking and listening to light: the evolution of whole-body photonic imaging.*, Nat Biotechnol **23** (2005), no. 3, 313–320 (eng).

10. Christopher C. Paige and Michael A. Saunders, *LSQR: An algorithm for sparse linear equations and sparse least squares*, ACM Trans. Math. Softw. **8** (1982), no. 1, 43–71.

11. G. Pratx, C.M. Carpenter, C. Sun, and Lei Xing, *X-ray luminescence computed tomography via selective excitation: A feasibility study*, Medical Imaging, IEEE Transactions on **29** (2010), no. 12, 1992–1999.

12. Michael Reed and Barry Simon, *Methods of modern mathematical physics. III*, Academic Press, New York, 1979, Scattering theory. MR MR529429 (80m:81085)

13. M Schweiger, SR Arridge, M Hiraoka, and DT. Delpy, *The finite element method for the propagation of light in scattering media: boundary and source conditions*, Med Phys **22(11 Pt 1)** (1995), 1779–92.

14. Plamen Stefanov and Gunther Uhlmann, *Linearizing non-linear inverse problems and an application to inverse backscattering*, J. Funct. Anal. **256** (2009), no. 9, 2842–2866. MR MR2502425

15. ———, *Thermoacoustic tomography with variable sound speed*, Inverse Problems **25** (2009), no. 7, 075011, 16. MR MR2519863

16. Ge Wang, Wenxiang Cong, Kumar Durairaj, Xin Qian, Haiou Shen, Patrick Sinn, Eric Hoffman, Geoffrey McLennan, and Michael Henry, *In vivo mouse studies with bioluminescence tomography.*, Opt Express **14** (2006), no. 17, 7801–7809 (eng).

17. Lihong V. Wang and Song Hu, *Photoacoustic tomography: in vivo imaging from organelles to organs.*, Science **335** (2012), no. 6075, 1458–1462 (eng).

18. Ashley J. Welch and Martin J.C. van Gemert (eds.), *Optical-thermal response of laser-irradiated tissue*, Springer, 2011 (English).

DEPARTMENT OF MATHEMATICS, PURDUE UNIVERSITY, WEST LAFAYETTE, IN 47907

DEPARTMENT OF BIOMEDICAL ENGINEERING, RENSSELAER POLYTECHNIC INSTITUTE, TROY, NY 12180

DEPARTMENT OF BIOMEDICAL ENGINEERING, RENSSELAER POLYTECHNIC INSTITUTE, TROY, NY 12180